

## *Chapter 5: Case Study for Magnesium Alloy Sheets to Predict Ductile Fracture of Rotational Incremental Forming*

### **5.1 Introduction**

As the lightest structural alloys, magnesium alloys have many advantages compared with steel, cast iron and even aluminum alloys [85]. However, the structural use of magnesium alloys is seriously restricted by their limited ductility at room temperature (RT) due to their hexagonal close-packed (HCP) crystal structure [86, 87].

At present, the magnesium alloys used for automobile parts are mainly processed by die casting [88, 89] that allows parts with complex geometry to be manufactured. Yet, the mechanical properties of such die cast parts invariably lack the required endurance strength and ductility [90]. As an alternative, the required mechanical properties for magnesium alloys can be achieved using a forming process instead of a die casting process. Parts manufactured by forming can have a fine-grained structure without porosity and improved mechanical properties, such as endurance strength and ductility [91]. Thus, research on mass produced magnesium alloy sheets has increased.

To widen the application of the alloys, researches on sheet forming of magnesium alloys at elevated temperatures has been made in several papers [90, 92, 93, 94]. Won *et al.* [95] investigated the mechanical properties of magnesium alloys at elevated temperatures and discovered that the Lankford value(R) for an AZ31 magnesium sheet decreases as the temperature increases. It was revealed that an AZ31 magnesium sheet becomes isotropic and re-crystallizes above 200°C. Won *et al.* [95] and Choo *et al.* [96] studied the formability of magnesium alloy sheets at high temperatures and concluded that a temperature over 200°C was required to achieve the safe forming of magnesium alloy sheets. Park *et al.* [97] studied and showed the possibility of cup incremental forming of magnesium sheet at room temperature with rotational, where the tool rotates itself. Their study show that even though the incremental sheet forming has been found to improve the forming limit for aluminum and steel sheets compared with press forming [59, 77], there has been little investigation of incremental sheet forming for magnesium because it is difficult to form at room temperature. Therefore, they proposed rotational incremental sheet forming (RISF), which was proven to improve the formability of sheet materials compared with incremental sheet forming due to large amount of heat were generated in the contact area due to friction energy at the tool-specimen interface and plastic deformation energy by the shear deformation.

In this study, the rotational incremental forming of magnesium alloy sheet for various wall angle of square shape are simulated using ABAQUS/Explicit finite element code. As the ductile failure criterion, the Oyane's fracture criterion via VUMAT user material based on a combined kinematic/isotropic hardening law and Johnson-Cook model is used to predict fracture at elevated temperatures which was generated by rotational tool and friction energy at the tool-specimen interface. Firstly, a combined kinematic/isotropic hardening law is applied for uni-axial tension-compression test at room temperature to determine the scalar parameter  $\beta$  which make the best fit of stress-strain curves between (FE) simulation and experiment results of magnesium alloy sheet. Johnson-Cook model is then utilized to predict the stress-strain curves at elevated temperatures and compared with measured values. Finally, based on the relationship between heat generation at the tool-specimen interface and various wall angles, the Oyane's fracture criterion is used to predict fracture for rotational incremental forming of magnesium alloy sheets. The effect of process parameters on ductile fracture value and forming limit curve at fracture were also investigated.

## 5.2 Finite element procedures

In FEM simulation, due to asymmetric yield surface, the uniaxial-stress-plastic-strain response of the material for the uni-axial compression test is assumed as Equation (5.1):

$$\bar{\sigma}^C = \frac{\sigma_Y^C}{\sigma_Y^T} K (\varepsilon_0 + \varepsilon_{eq}^{pl})^n \quad (5.1)$$

Where K is the plastic coefficient,  $\sigma_Y^T, \sigma_Y^C$  are tension and compression yield stress, n is the work-hardening exponent, and  $\bar{\sigma}^C, \bar{\varepsilon}_{eq}^{pl}, \varepsilon_0$  are the equivalent stress in compression zone, equivalent strain, and yield strain, respectively, which were mentioned in Table 5.1.

**Table 5.1:** Maximum temperature of the tool and specimen for each square cup (Ref. [97])

Wall angle, $\theta$ (°)	Temperature of tool, (°C)	Temperature of specimen, (°C)
45	105	100
60	125	118
70	150	141

Figure 5.1 shows the stress-strain curves obtained from the in-plane uni-axial compression and tension tests at room temperature. Figure 5.2 shows experimental results for the yield loci, which were not symmetric, and the compressive behavior differed from the tensile behavior. These phenomena were unique behavior of magnesium alloy sheet because of its crystal structure.

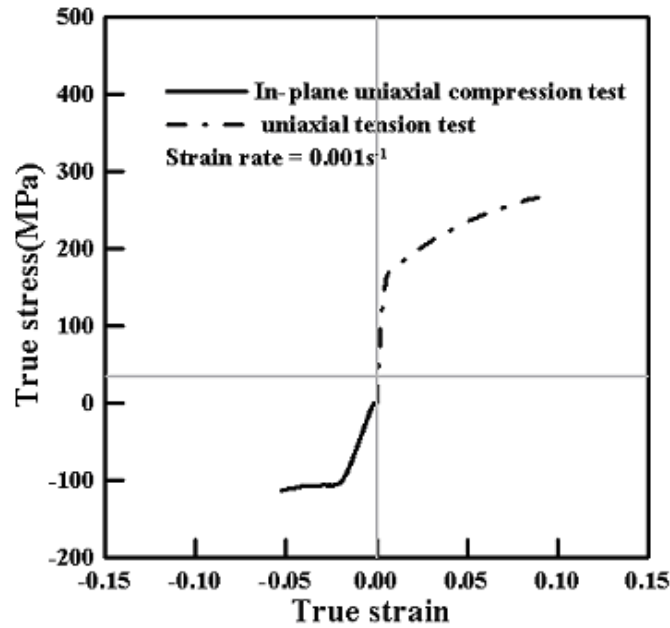


**Figure 5.1:** Stress-strain curves obtained from in-plane uniaxial compression tests at room temperature (Ref. [97])

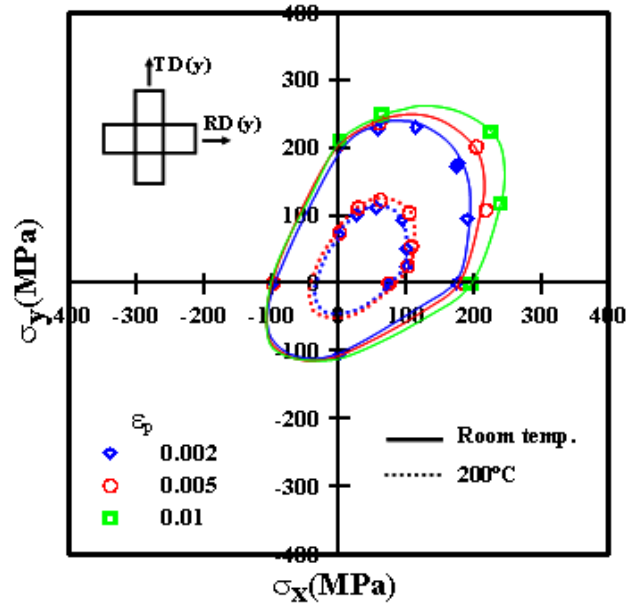


**Figure 5.2:** Yield loci obtained from biaxial tensile tests and in-plane uniaxial compression tests (Ref. [97])

In this chapter, due to low average R-value (Lankford value) at elevated temperature ( $R \sim 1$  at  $200^\circ\text{C}$ ), the Von-Mises model was assumably applied in calculation.

### 5.2.1 Johnson–Cook model at elevated temperatures

The inelastic behavior of the investigated alloy is assumed to be described by Johnson–Cook model [98]. This material model is suited to describe the mechanical behavior of material at high strain rates and various temperatures. It is generally used in adiabatic transient dynamic analysis. The hardening is a particular type of isotropic hardening in which the yield stress  $\bar{\sigma}$  is assumed to be of the form:

$$\bar{\sigma} = (A + B(\varepsilon_{eq}^{pl})^n) \left( 1 + C \log \left( \frac{\dot{\varepsilon}_{eq}^{pl}}{\dot{\varepsilon}_0} \right) \right) (1 - \hat{T}^m) \quad (5.2)$$

where

$$\hat{T} = \begin{cases} 0 & \text{for } T < T_r \\ \frac{T-T_r}{T_m-T_r} & \text{for } T_r \leq T \leq T_m \\ 1 & \text{for } T > T_m \end{cases} \quad (5.3)$$

$A$ ,  $B$ ,  $C$ ,  $n$  and  $m$  are material parameters, to be identified.  $T$  is the current temperature,  $T_m$  is the melting temperature and  $T_r$  is a reference temperature of 24 °C.

In this study, we verify the unusual plastic behavior for magnesium sheet at elevated temperatures with constant strain rate ( $\dot{\varepsilon}_0 = \dot{\varepsilon}_{eq}^{pl}$ ). Besides, the stress-strain curve has been fitted as in Equation 3.1. So that Equation (5.2) can be expressed as following reduced form

$$\bar{\sigma} = K(\varepsilon_0 + \varepsilon_{eq}^{pl})^n \left( 1 - \left( \frac{T-T_r}{T_m-T_r} \right)^m \right) \quad (5.4)$$

To determine  $m$  quasi static experimental results at both room and higher temperatures are needed. If quasi static experiments, at the same strain rate, are carried out at two different temperatures denoted by the superscripts (5.2) and (5.3), the ratio  $r$  between the stresses at a specific plastic strain can be expressed as:

$$r = \frac{\bar{\sigma}^{(1)}(\varepsilon_{eq}^{pl})}{\bar{\sigma}^{(2)}(\varepsilon_{eq}^{pl})} = \frac{1 - (\hat{T}^{(1)})^m}{1 - (\hat{T}^{(2)})^m} \quad (5.5)$$

If  $T^{(2)} = T_r$  then from Equation (5.2)  $\hat{T}^{(2)} = 0$  and  $m$  is given by

$$m = \frac{\log(1-R)}{\log(\hat{T}^{(1)})} \quad (5.6)$$

The stresses shown in Figure 5.3 for temperatures 100 °C, 150 °C and 200 °C are divided by the stresses at 24 °C (room temperature) according to Equation (5.5). The result is as well as the average values in the range  $0.05 < \epsilon^l < 0.25$ . The averaged values are  $r = 0.879$ ,  $r = 0.712$  and  $r = 0.444$  for 100 °C, 150 °C and 200 °C respectively. Substituting these values into Equation (5.6) results in  $m = 1.027$  for 100 °C,  $m = 0.802$  for 150 °C, and  $m = 0.48$  for 200 °C.

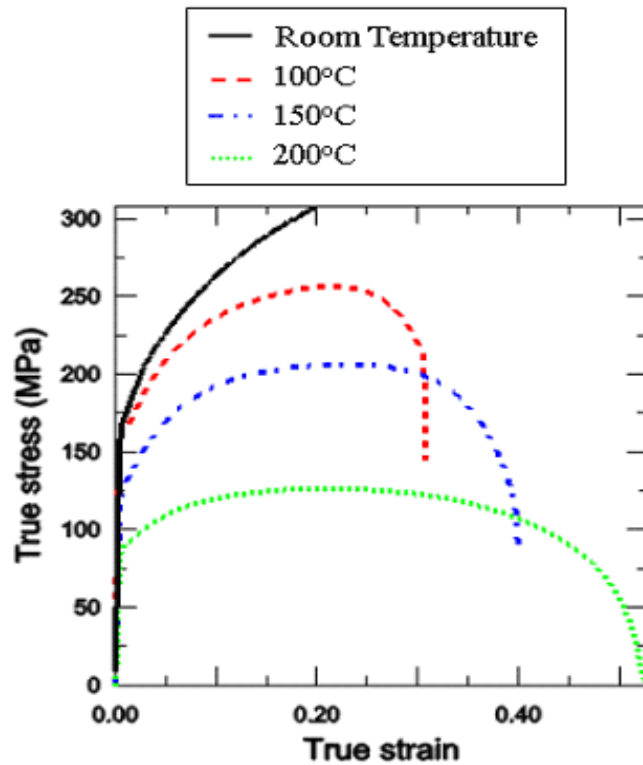


Figure 5.3 The stress-strain curves with measured values [97]

By adopting Johnson–Cook model thought using Equation (5.7) instead of Equation (3.1) in VUMAT subroutine for tensile test simulation at 100 °C, 150 °C and 200 °C we can obtain the FE simulation results in Figure 5.4

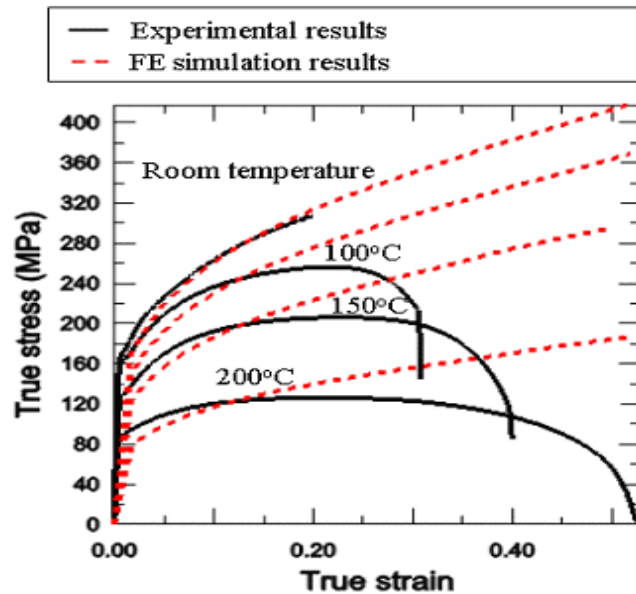


Figure 5.4: The stress-strain curves calculated using FE simulation and compared with the measured values

### 5.2.2 Problem description, geometry and FE models for rotational incremental forming of magnesium alloy sheet

In this study, we applied above model for square shape rotational incremental forming of magnesium alloy sheet. Here, the specimens were 150 mm (width) by 150 mm (length) by 1 mm (thickness). Meanwhile, the experimental model of the square shape was 80 mm (width) by 80 mm (length) by 25 mm (height). The depth increment was 0.4 mm in the z-direction, and the wall angles of the square cup shape were determined as 45 °, 60 °, and 70 °, respectively. The tool radius was 6mm and the feed rate was 400mm/min. As following previous study [97], in experiment the spindle speed of the tool was 4000 rpm on count clock wise for -z-direction until the temperature of the tool was 100 ° C in case of 45 ° wall angle and then set to 3000 rpm. Due to the temperature of the tool exceeded 100°C, chips of magnesium were generated in the contact area between the specimen and the tool. Therefore, 100 ° C is maximum temperature in case of 45 ° wall angle without chip generating. As same way, for the other case, maximum temperature was measured while Table 5.2 shows the maximum temperature of the tool and specimen for each square cup.

**Table 5.2:** Thermo-physical properties of magnesium alloy AZ31 as function of temperature  $T$  (in ° C) [99]

Thermo-physical property	AZ31
Thermal conductivity (W/(m K))	$77 + 0.096 T$
Specific heat capacity (J/(kg K))	$1000 + 0.666T$
Thermal coefficient expansion (K <sup>-1</sup> )	2.48e-05

As previous experiments [97], no fractures were observed with the 45 ° wall angle but fractures were observed with the 70° wall angle (Figure 5.5). The minor and major strains of a, b, c, d, and e in Figure 5.5 (c) were measured and represented as shown in Figure 5.6. Here, the open symbol of ( $\Delta$ ,  $\square$ ,  $\circ$ ) represents the strain with 45 °, 60 °, 70 ° wall angles and no fractures. Otherwise, the cross symbol ( $\times$ ) represents the occurrence of a fracture in wall and corner areas with a 70 ° wall angle.

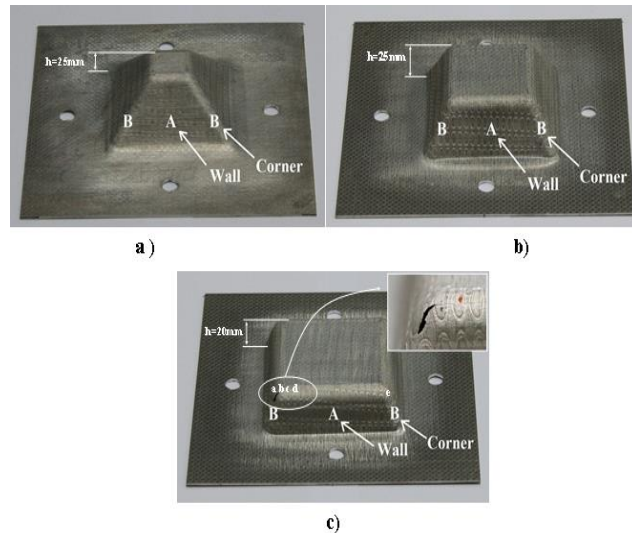


**Figure 5.5:** The square cups formed by rotational incremental sheet forming of (a) 45° wall angle, (b) 60° wall angle, and (c) 70° wall angle at which the crack was occurred (Ref. [19]).

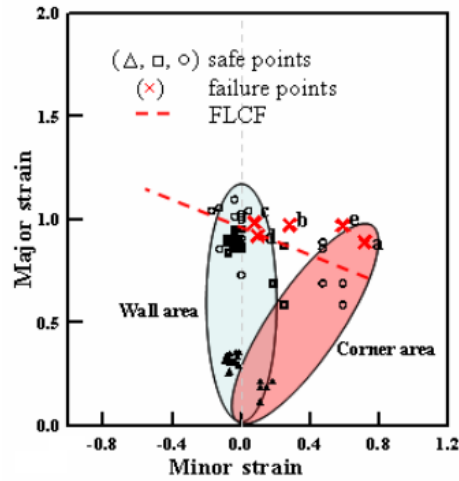


**Figure 5.6:** Forming limit for rotational incremental forming

As mention from the previous literature [59, 77], most forming limit curves in incremental sheet forming (FLC at fracture: FLCF) appears to be a straight line with a negative slope in the positive region of the minor strain. By adopting this linear model (Figure 5.6) to formulate a forming limit curve (FLCF), it can be expressed as follow:

$$\varepsilon_1 + 0.639\varepsilon_2 = 1.02 \quad (5.7)$$

Figure 5.7 shows the finite-element model for the incremental sheet forming test process. To simulate the experiments, only one quarter of specimen is modeled, the blank modeled using solid elements C3D8R, the punch modeled using analytical rigid surface-elements, and the die modeled using rigid surface-elements R3D4. Throughout this study, the average element size of the blank was about 1 mm in width, 1mm in length, and 0.33 in thickness; the average element size of the rigid die was about 2 mm in width, and 2 mm in length. Here, the die was fixed in all directions. The tool was allowed to move following the tool-path and rotate involving z direction at the centre point of the tool. The friction behavior was modeled using the Coulomb friction law. The friction coefficient  $\mu_1$  between the blank and the punch is assumed to be the same the fiction coefficient  $\mu_2$  between the blank and the die of 0.1. The other physical properties of the materials used in the analysis are shown in Table 5.2.

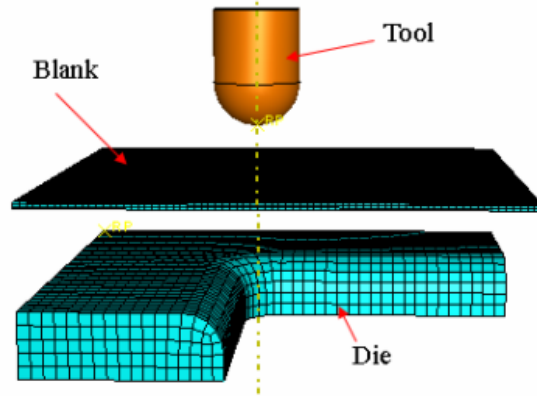


**Figure 5.7:** Finite element model for incremental forming simulation

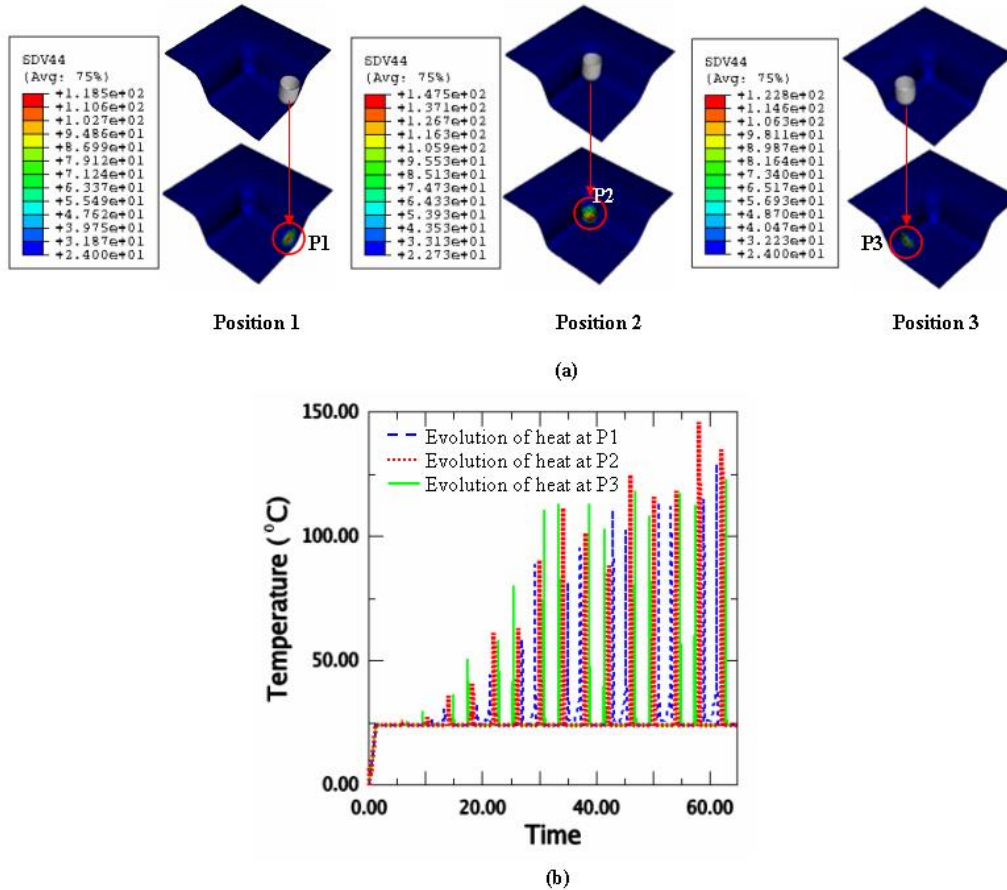
### 5.2.3 Ductile fracture criterion

To determine the material constants  $C_1$ ,  $C_2$  in Equation (3.3), destructive tests have to be operated under at least two types of stress conditions. Here, we utilized forming limit curve at fracture Equation (5.7) to calculate the fracture strain for uni-axial tension and a plane strain state as 1.499 and 1.178, respectively. From this result, the material constants  $C_1$ , and  $C_2$  for the ductile fracture criterion were calculated as 2.059, and 3.586, respectively.

Oyane's the ductile criterion in Equation (5.8) is combined with proposed hardening model and Johnson-Cook model, and then coded into a VUMAT subroutine.

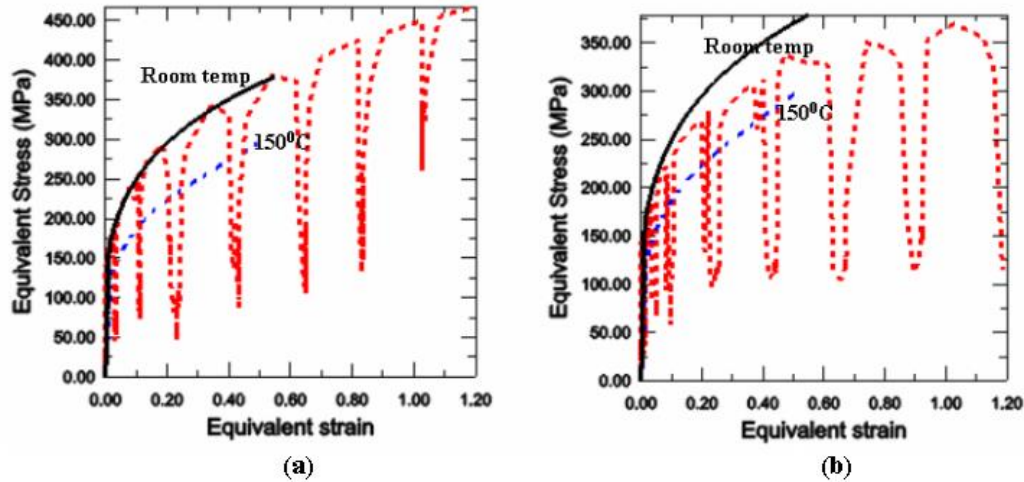
### 5.3 Results and discussion

Figure 5.8 (a) shows the FE simulation results of heat generation (SDV44) in the contact area between the specimen and the tool for three different positions of tool, Figure 5.8 (b) depicts the evolutions of temperature at the elements corresponding to three tool positions of Figure 5.8 (a) for the case of  $70^\circ$  wall angle.



**Figure 5.8:** Heat generation in the contact areas between the specimen and the tool

The results show that the maximum temperatures in FE simulation of 147 °C at corner and about 122 °C at wall areas are good agreement with that in experimental measurement of 141 °C given in Table 5.1. In order to verify the effect of heat generation on the stress-strain curve without considering Johnson-Cook model, equivalent stress-strain evolution in incremental forming, obtained by (FE) simulation via VUMAT user material, were compared with other stress-strain curves at elevated temperatures obtained by adopting Johnson–Cook model for tensile test simulation in Figure 5.4 and shown in Figure 5.9 (a).



**Figure 5.9:** Evolution of equivalent stress-strain curve in incremental forming in case of (a) without considering Johnson-Cook model and (b) considering Johnson-Cook model

Even though the (FE) simulation predicts well heat generation, the boundary profile of equivalent stress-strain evolution in incremental forming without considering Johnson-Cook model was still following stress-strain curve at room temperature. So that, in this study, heat generation at elements in the contact area between the specimen and the tool was calculated considering Johnson-Cook model using Equation (5.4) and coded into VUMAT subroutine for incremental forming simulation. The equivalent stress-strain evolution in this case was shown in Figure 5.9(b). The boundary profile of equivalent stress-strain evolution, which was limited by stress-strain curves at room temperature and 150 °C in tensile test simulation, proved the effect of heat generation on stress-strain curve and was suitable with experiments of tensile test at elevated temperatures. This method should be applied to predict ductile fracture in (FE) simulation of rotational incremental forming of magnesium alloy.

The (FE) simulation results for three cases test sample with the equivalent plastic strain  $\bar{\epsilon}$  (SDV7), and the maximum ductile fracture value  $I$  (SDV9) calculated from Equation (25) via VUMAT user material based on a combined kinematic/isotropic hardening law are presented in Figure 5.10. The simulation results show that the maximum value of the fracture ductile integral  $I$  of the (80 mm × 80 mm × 25 mm) square shape with 40°, and 60° wall angles

corresponding 105 °C, and 126 °C of maximum temperature are 0.513 and 0.898, respectively, which is smaller than 1.00. This means that failure do not occur in this case of process. Otherwise, in case of the (80 mm × 80 mm × 20 mm) square shape with 70 ° wall angle corresponding 147 ° C of maximum temperature, the (FE) simulation results give the maximum value of ductile fracture integral  $I$  equal to 1.242, and failure appeared. The trends of the failure site predicted in his study were in quite good agreement with those in the actual experiments.

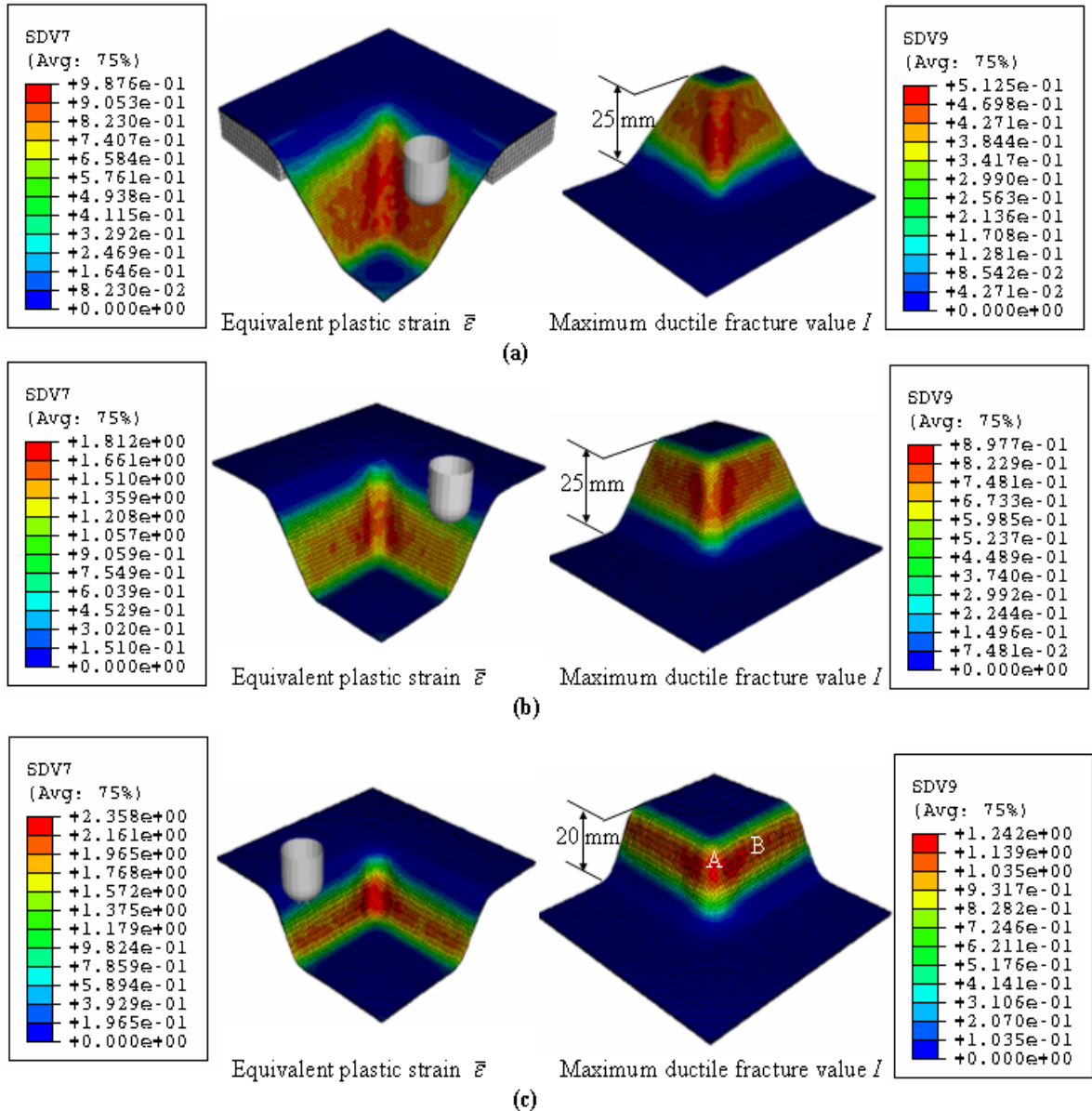
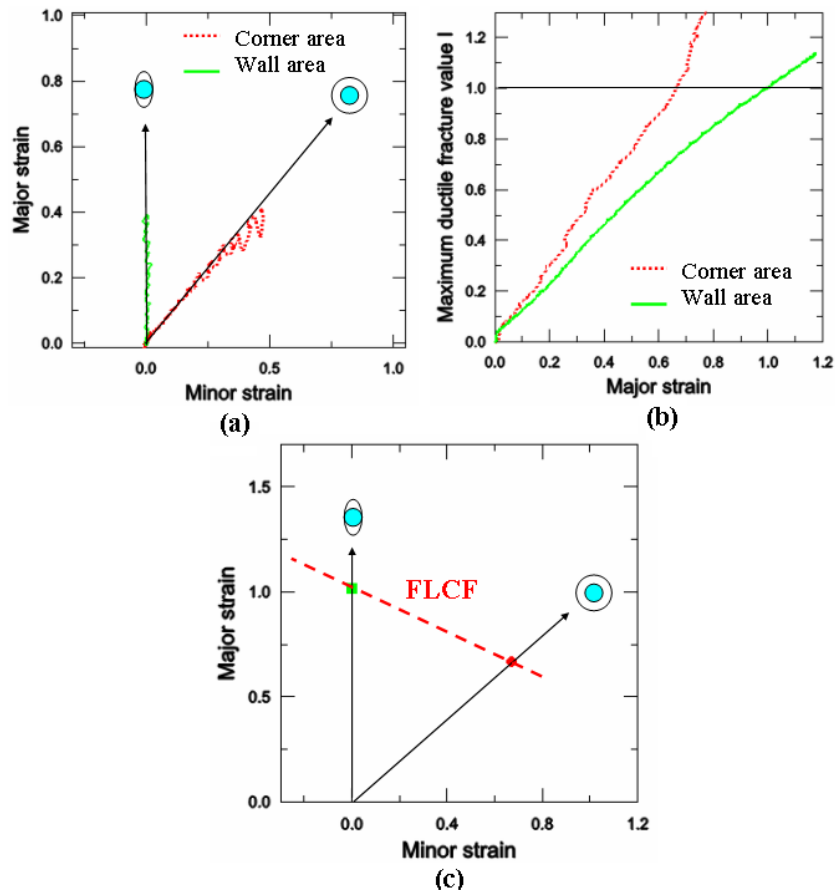


Figure 5.10: Deformed shape in finite element simulation in case of (a) 45° wall angle, (b) 60° wall angle, and (c) 70° wall angle

After the simulation, it can be concluded that in order to obtain a sound final product, the wall angle of the square shape should be smaller than  $70^\circ$ . Even though the heat generation is smaller than the case of  $70^\circ$  wall angle,  $45^\circ$  and  $60^\circ$  wall angles can be deformed to the final shape without any failure.

In order to predict forming limit curve at fracture utilized (FE) simulation results, we proposed the method as shown in Figure 5.11. Figure 5.11 (a) shows the evolutionary strain paths at the element of corner area (point A in Fig 5.10 (c)) and the element of wall area (point B in Figure 5.10 (c)). These strain paths is suitable to the paths of equal biaxial stretching and plane strain. Figure 5.11 (b) presents the evolutions of the ductile fracture integral  $I$  at the elements of concerned points (A and B) versus major strain. From Figure 5.11 (b), the major strains at occurred fracture ( $I = 1$ ) of concerned points of equal biaxial stretching and plane strain are determined as 0.665 and 1.017, respectively. Figure 5.11 (c) depicts the forming limit curve at fracture (FLCF) obtained by adopting a linear model through occurred fracture points from (FE) simulations. This (FLCF) is quite good agreement with the previous assumption of Equation (5.7) and Figure 5.6.



**Figure 5.11:** FLCF obtainment from FE simulation at the corner and wall area for the case of  $70^\circ$  wall angle.

### 5.3.1 Effect of tool down-step

To verify the effect of tool down-step ( $H$ ), analysis is carried out for the tool down-step ( $H$ ) of 0.8 mm, and 1.2 mm and then results are compared with that of  $H = 0.4$  mm discussed earlier for the case of the (80 mm  $\times$  80 mm  $\times$  20 mm) square shape with 70° wall angle corresponded 140 °C of temperature and the tool radius ( $R$ ) of 6 mm. As shown in Figure 5.12, the maximum values of ductile fracture integral  $I$  in these cases are predicted to be 1.271 and 1.324, respectively. Thus, at higher tool down-step, the maximum values of ductile fracture integral  $I$  will be larger. This happens, because deformation becomes larger with increase in tool down-step.

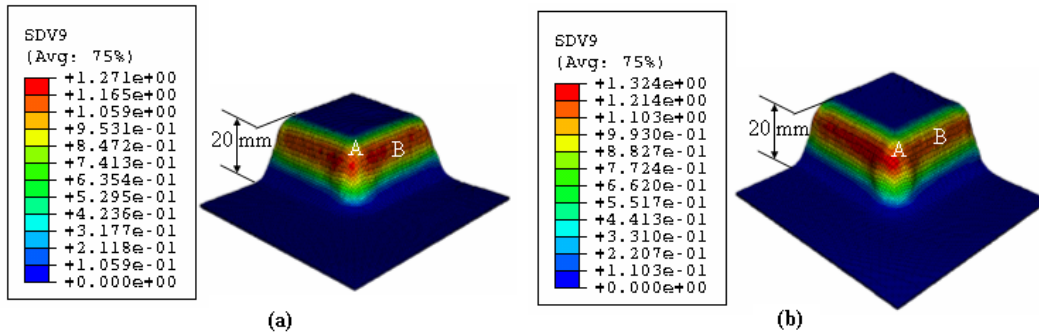


**Figure 5.12:** Deformed shape in FE simulation in case of 70° wall angle, tool radius of 6 mm, and (a) tool down-step of 0.8 mm; (b) tool down-step of 1.2 mm

Figure 5.13 presents the (FLCF) obtained by adopting a linear model through occurred fracture points ( $I = 1$ ) of equal biaxial stretching and plane strain for all three cases. When the down-step increased from 0.4 mm to 0.8 mm, and 1.2 mm, the fracture major strains of equal biaxial stretching and plane strain decreased to 0.613, 0.544 and 0.94, 0.85, respectively, so that the (FLCF) moved down. Thus, it is clear that the formability becomes lower as the down-step becomes higher. These results were similar to the experimental results and conclusions of previous study [77].

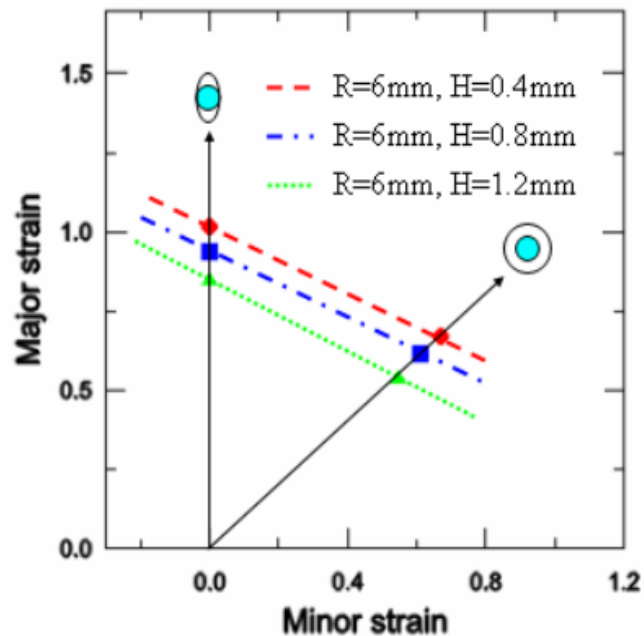


**Figure 5.13:** FLCF with different tool down-step and 6 mm tool radius

### 5.3.2 Effect of tool radius

The effect of tool radius ( $R$ ) is investigated by carrying out the analysis for the following two cases of  $R = 4$  mm, and 8 mm. The analysis is carried out for the case of the (80 mm  $\times$  80 mm  $\times$  20 mm) square shape with 70° wall angle and the tool down-step ( $H$ ) of 0.4 mm. The maximum values of ductile fracture integral  $I$  was found to be 1.229, and 1.258, respectively as shown in Figure 5.14. Figure 5.15 depicts the (FLCF) when the tool radius changes from 6 mm to 4 mm and 8 mm. The (FLCF) is lower in case of 8mm tool radius with the fracture major strains of equal biaxial stretching and plane strain is 0.614, and 0.927, respectively. In the case of 4 mm tool radius, the fracture major strain increased to 0.717 at equal biaxial stretching and decreased to 0.597 at plane strain area. As the tool radius increases, the deformation zone or the contact zone increases, and the level of strain decreases resulted incremental formability.

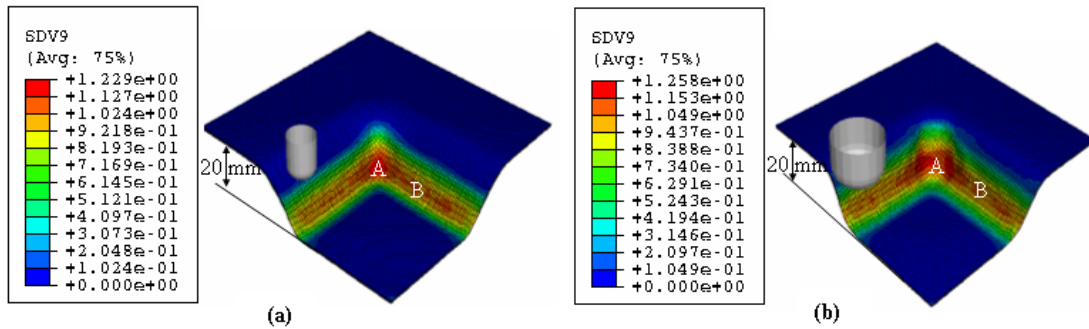


**Figure 5.14:** Deformed shape in FE simulation in case of 70° wall angle, tool down-step of 0.8 mm, and (a) tool radius of 4 mm; (b) tool radius of 8 mm

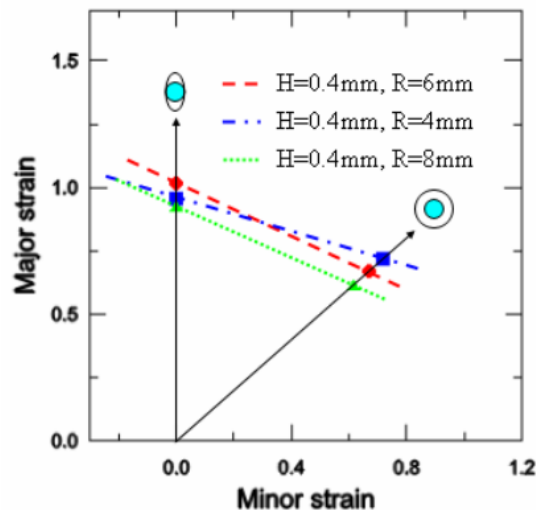


**Figure 5.15:** FLCF with different tool radius and 0.4 mm tool down-step

## 5.4 Conclusion

In this study, to predict a fracture of rotational incremental forming for magnesium alloy sheet, the heat generation at elements due to rotational tool and contact area between the specimen and the tool was implemented using finite element simulations through Johnson-Cook model and then compared with experiments of the square shape with 45 °, 60 °, and 70 ° wall angles. Commercial software (ABAQUS version 6.5, explicit formulation) with a user-defined subroutine (VUMAT) based on a combined kinematic/isotropic hardening model was used for the simulation. The (FE) simulation results show that if the wall angles of 80 mm × 80 mm × 25mm square shape are smaller than 60 ° then the maximum value of the fracture ductile integral  $I$  will be less than 1 value, and fracture will not occur. The predictions of failure site were in good agreement with those in actual experiments. The (FLCF) prediction and effect of process parameters on (FLCF) utilized (FE) simulation results show that the formability decreases as the tool down-step or tool radius increase. This prediction is suitable to previous conclusion [77] of incremental sheet forming process.